

1 **Supplementary Information**

2 **An evaluation of new particle formation events in Helsinki during a Baltic Sea cyanobacterial**
3 **summer bloom**

4
5 Roseline C. Thakur¹, Lubna Dada^{1,2,3}, Lisa J. Beck¹, Lauriane L.J. Quéléver¹, Tommy Chan¹, Marjan
6 Marbouti^{1,12}, Xu-Cheng He¹, Carlton Xavier¹, Juha Sulo¹, Janne Lampilahti¹, Markus Lampimäki¹,
7 Yee Jun Tham^{1,11}, Nina Sarnela¹, Katrianne Lehtipalo^{1,4}, Alf Norkko^{8,9}, Markku Kulmala^{1,5,6,7}, Mikko
8 Sipilä¹, Tuija Jokinen^{1,10}

9
10 ¹Institute for Atmospheric and Earth System Research/Physics, Faculty of Science, 00014 University
11 of Helsinki, Helsinki, Finland.

12 ²School of Architecture, Civil and Environmental Engineering, École Polytechnique Fédérale de
13 Lausanne, Lausanne, Switzerland

14 ³Laboratory of Atmospheric Chemistry, Paul Scherrer Institute, 5232 Villigen PSI, Switzerland

15 ⁴Finnish Meteorological Institute, Helsinki, Finland.

16 ⁵Aerosol and Haze Laboratory, Beijing Advanced Innovation Center for Soft Matter Science and
17 Engineering, Beijing University of Chemical Technology, 100089 Beijing, China.

18 ⁶Joint International Research Laboratory of Atmospheric and Earth System Sciences, Nanjing
19 University, 210023 Nanjing, China.

20 ⁷Lomonosov Moscow State University, Faculty of Geography, 119991, Moscow, GSP-1, 1
21 Leninskiye Gory.

22 ⁸Tvärminne Zoological Station, University of Helsinki, J.A. Palméns väg 260, FI-10900 Hangö,
23 Finland .

24 ⁹Baltic Sea Centre, Stockholm University, Stockholm, Sweden

25 ¹⁰Climate & Atmosphere Research Centre (CARE-C), The Cyprus Institute, P.O. Box 27456, Nicosia,
26 CY-1645, Cyprus.

27 ¹¹School of Marine Sciences, Sun Yat-Sen University, Zhuhai 519082, China.

28 ¹² Department of Electronics and Nano-engineering, Aalto University, 00076 Aalto, Finland.

29

30

31

32 **Back trajectory calculations**

33 Back trajectories of the different NPF event days were calculated using the data from the Global data
34 Assimilation System (GDAS) as input into the NOAA Hybrid Single-Particle Lagrangian Integrated
35 Trajectory (HYSPLIT) model (<http://www.arl.noaa.gov/ready/>, Rolph et al., 2017; Stein et al., 2015).
36 We used the isentropic trajectories as they incorporate vertical transport components. The 24 h back
37 trajectories were calculated at an arrival height of 100 m a.g.l. The new trajectory starts every 6 hours.
38 The frequency (%) of trajectory was calculated with the following equation (Eq. (1)).

39

$$\text{Traj. Freq.} = \frac{100 \times \text{number of trajectories passing through each grid square}}{\text{number of trajectories}} \quad (1)$$

40 The trajectory analysis was also performed using the Lagrangian particle dispersion model Flexpart
41 v10.4 (Pisso et al., 2019; Stohl et al., 2005) mainly to assess the residence times of the air masses.
42 Flexpart is a stochastic model used to compute trajectories of hypothetical particles, based on mean
43 as well as turbulent and diffusive flow (Pisso et al., 2019). We have used Flexpart along with ECMWF
44 ERA-Interim wind-fields which has a spatial resolution of $1^\circ \times 1^\circ$ at three hour temporal resolution
45 (Pisso et al., 2019). Flexpart was used to simulate 3-day backward trajectories starting from the
46 particle release point located at SMEAR III (24.5° E, 60.1° N) for the event days. The residence times
47 were normalized for clarity in the all the figures and is shown on a scale of 0 to 1.

48 **Meteorological and other supporting data**

49 The meteorological data such as wind speed, wind direction, temperature, pressure, relative humidity
50 and other supporting datasets e.g chlorophyll (Chl-*a*), SO₂, O₃ concentration and sea level information
51 was additionally used to interpret the NPF events and support the observations of this work (See table
52 S1 for details). All the meteorological parameters are measured by sensors installed on the roof of the
53 physicum building (where CI-APiTOF was housed). Thus we can say that the precursor vapor
54 concentrations measured by the CI-APiTOF was not influenced by any vertical mixing of airmasses
55 since the sensors for meteorological parameters (installed on the roof of 5th floor, physicum building
56 and CI-APiTOF (installed on the 4th floor, physicum building) was almost at the same height.
57 However, the measurements for particle size distributions was carried out at SMEAR III, which is 25
58 m a.m.s.l and the wind vane at the physicum building was situated roughly at 50 m a.m.s.l. ,we state
59 that the particle size distribution data might not be completely free from downward vertical mixing
60 of airmass and should be treated with certain uncertainty. However, near the SMEAR III station, the

61 mixing usually affected the larger particles, decreasing their number concentration (Järvi et al., 2009).
62 So we can assume that the uncertainties in the number concentration of nucleation and Aitken mode
63 particles would be negligible in this study.

64 The Chl-*a* satellite images were mapped through the GlobColour level-3. The GlobColour level-3
65 mapped products present merged data from SeaWiFS, MERIS, MODIS AQUA, VIIRS (O'Reilly et
66 al., 2000) sensors to provide robust and high coverage data for Chl-*a* measurements. The merging
67 processes are described in Mangin and d'Andon, 2017. In this study, weighted average method
68 (AVW) for retrieving daily Chl-*a* concentration (mg m^{-3}) for latitude: 45 °N to 80 °N and longitude:
69 20 °W to 60 °E was used. The GlobColour level-3 binned products have a resolution of $1/24^\circ$ at the
70 equator (i.e. around 4.63 km) for global products (Mangin and d'Andon, 2017). The details of these
71 additional supporting data given in SI (Table S1). However this resolution is not high enough to
72 demarcate the contribution of Chl-*a* from cyanobacteria and macroalgae in the marine region.
73 Nonetheless, the contribution of macroalgae to Chl-*a* still holds a significant place since the Baltic Sea
74 and other regions of Gulf of Finland are abundant in microalgae.

75 **Formation and growth rate calculations**

76 The growth rates (GRs) were calculated based on the 50% appearance time method using the NAIS
77 ion data from both polarities, depending on the better quality polarity (Dada et al., 2020; Dal Maso et
78 al., 2016; Lehtipalo et al., 2014). This method uses particle number concentration at different size
79 bins (D_p), which are recorded as a function of time. The “appearance time” of particles of size D_p
80 is the time when their number concentration reaches 50% of its maximum value during the NPF event.
81 To estimate the maximum GR (kinetic) that can be explained by the condensation of certain vapors,
82 two parametrization methods were used, first by Nieminen et al., 2010 for IA and MSA and the
83 second by Stolzenburg et al., 2020 for SA. The growth estimation from SA condensation recently
84 provided by Stolzenburg et al., 2020 also takes into account the hydration of SA particles and dipole-
85 dipole enhancement which is responsible for increasing the collision rate between neutral molecules
86 and neutral particles. As these parameters were not known for IA and MSA, we used the method by
87 Nieminen et al. (2010) for them. The growth due to MSA could be slightly overestimation by this
88 method (Beck et al., 2021) since the parameterization is based on the assumption of irreversible
89 condensation, but MSA rapidly partitions between gas and particle phases if suitable meteorological
90 conditions prevail. The calculated kinetic GR was compared with the total measured particle GR to
91 determine the contribution of each vapor to the growth process (discussed in further sections).

92 The formation rate of the total particles of mobility diameter 1.5 nm is calculated using
93 the time derivative of the particle number concentration measured using the PSM in the size range
94 1.5– 3 nm. The formation rate was corrected for the coagulation losses and growth out of the bin
95 following the method explained by Kulmala et al. 2012. The formation rate of the charged particles
96 was calculated from the time derivative of ions measured using the NAIS in ion mode in size range
97 1.5–3 nm from both polarities. The formation rate of ions was corrected for coagulation sink, growth
98 outside of the bin, ion-ion recombination and ion-neutral attachment as previously discussed in
99 Kulmala et al. 2012.

100 **Table S1 Details of Instruments and other supporting data**

Parameter measured	Technique	Instrument	Resolution and detection limits	Site of Measurement
SO ₂	UV-fluorescence technique	Horiba APSA 360	60 s detection limit: 0.2 ppb	a
NO _x	Chemiluminescence technique + thermal (molybdenum) converter	TEI42S	60 s detection limit: 0.2 ppb	a
O ₃	IR-absorption photometer	TEI 49	60 s detection limit: 0.5 ppb	a
Air Temperature	Platinum resistance thermometer	Pt-100	60 s	b
Wind direction	2-D ultrasonic anemometer	Thies Clima ver. 2.1x	10 s	b
Wind Speed	Platinum resistance thermometer + thin film polymer sensor	Vaisala DPA500	4 min	b
Relative humidity	Platinum resistance thermometer + thin film polymer sensor	Vaisala DPA500	4 min	b
Global Radiation	Net radiometer	Kipp & Zonen CNR1	60s	b
Tidal Height	wave buoys		c	Helsinki Suomenlina, Gulf of Bothnia, Northern Baltic Sea

102

103 ^a SMEAR III station

104 ^broof of university of Helsinki (UHEL) Building (kumpula campus)

105 ^cWave height is the vertical difference between the wave trough and the wave crest. The
106 significant wave height is calculated as the average of one third of the highest waves from the
107 energy spectrum.

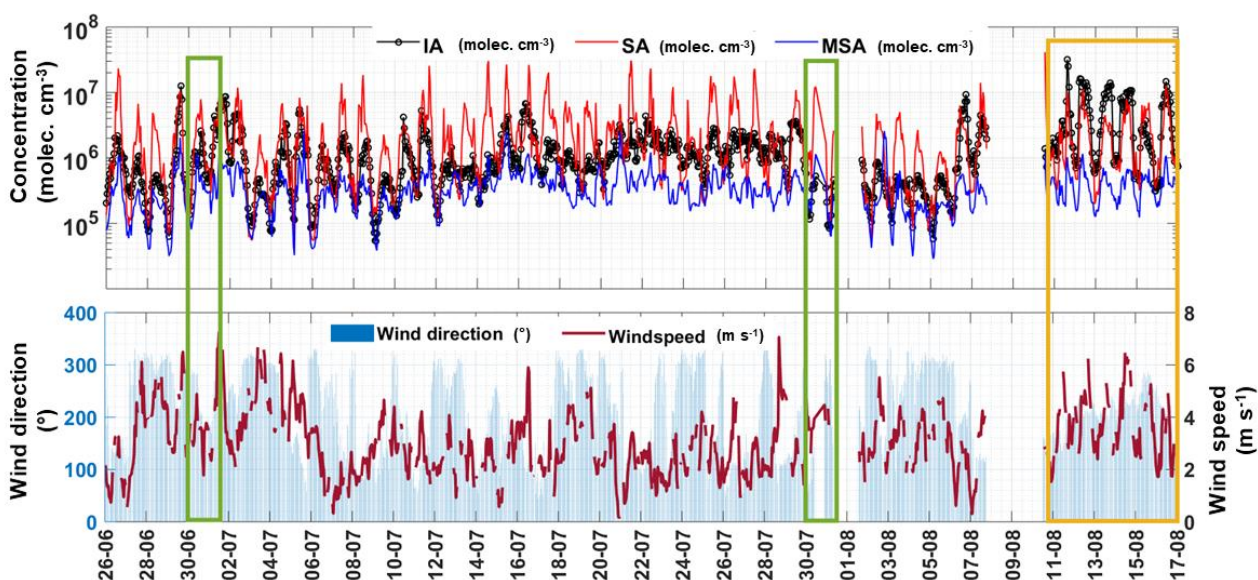
108

109 **The cloudiness parameter**

110 It is defined as is the ratio of measured global radiation (R_d) divided by the theoretical global
111 irradiance (R_g):

112
$$P = \frac{R_d}{R_g}$$

113 The theoretical maximum of global radiation (R_g) is calculated by taking into consideration the
114 latitude of the measurement station and the seasonal solar cycle. $P < 0.3$ defines a complete cloud
115 coverage and $P > 0.7$ defines clear-sky conditions. This classification is followed by man previous
116 studies (Perez et al., 1990; Sogacheva et al., 2008; Sánchez et al., 2012).

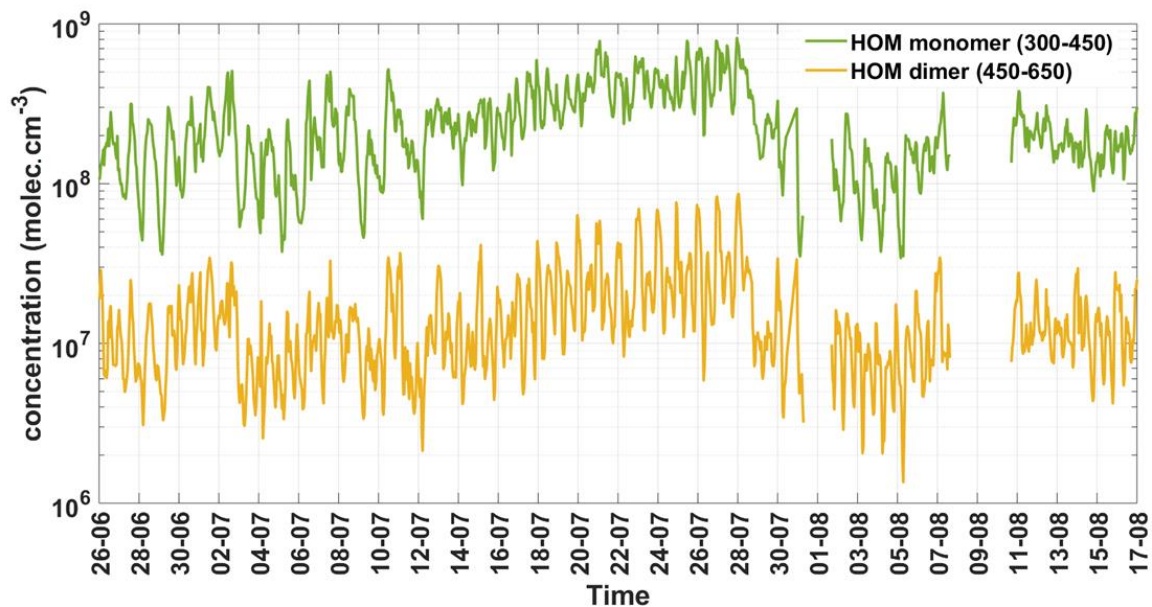


117

118 **Figure S1:** Time series concentration of SA, MSA and IA (60min averaged data) and their
119 variability with changing wind speed and wind direction (30min averaged data). The Green boxes

120 denote the local events and yellow box is covers the time period when the burst/spike events were
121 observed during the study.

122

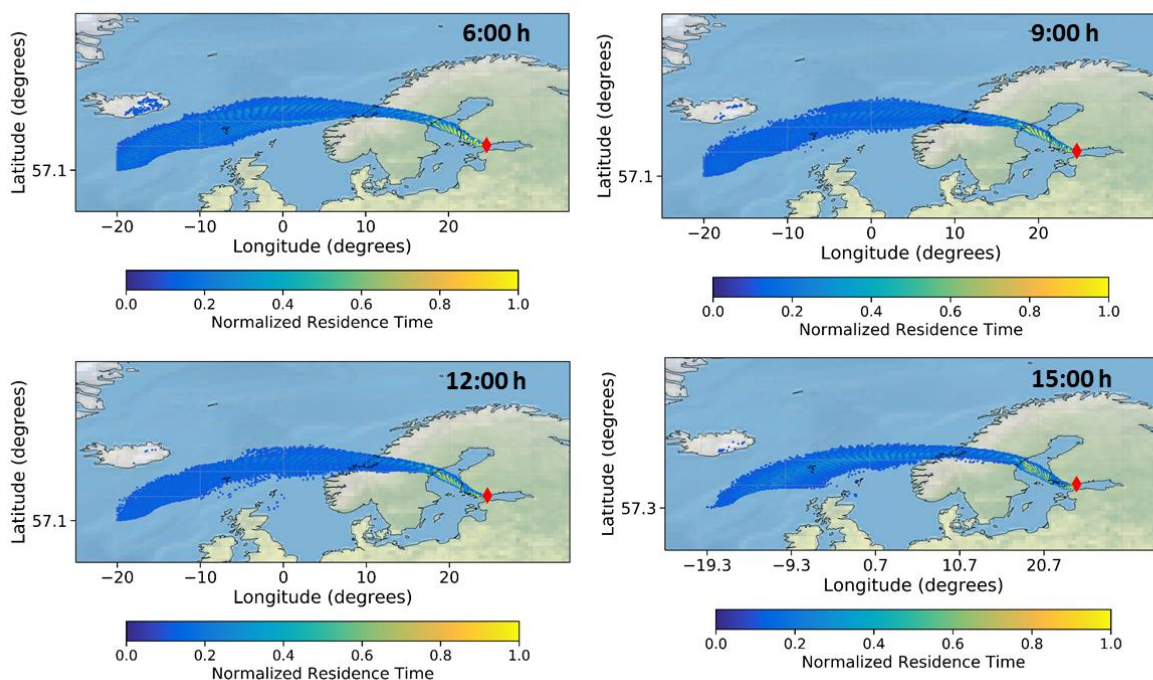


123

124

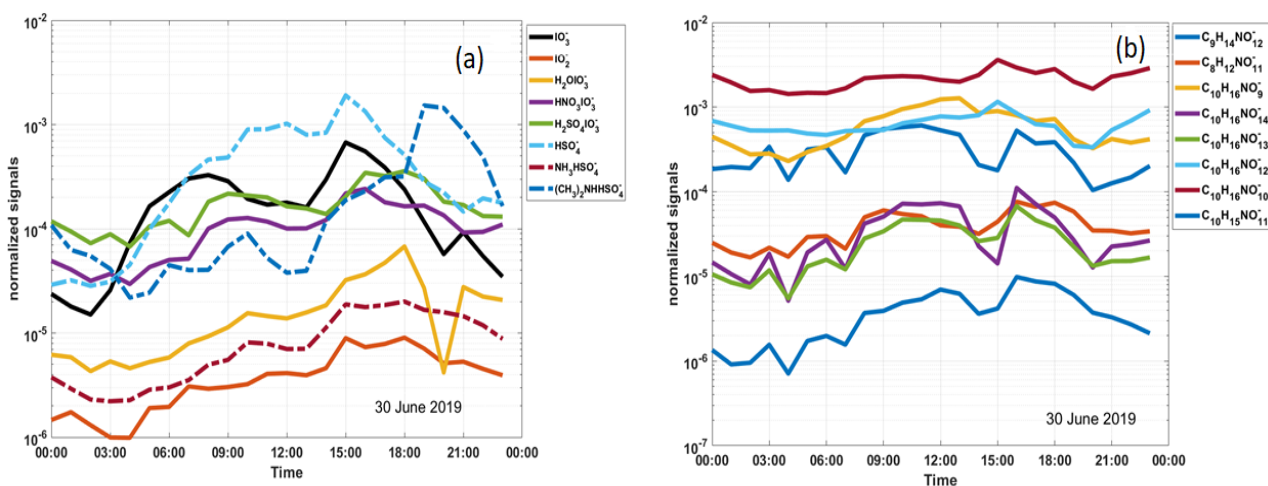
125 **Figure S2:** Time series variability in HOM monomer (sum of mass range 300-450 m/z) and dimer
126 (sum of mass range 450-650 m/z) concentration during the study period (60min averaged data from
127 CI-Api-ToF). Note the concentrations are plotted using the unit mass resolution data.

128



130

131 **Figure S3:** Normalized residence times of air masses (3-day backwards) arriving at the experimental
 132 site on 30 June 2019. The color bar indicates the normalized residence times for each subplot. The
 133 residence time of particles originating 3 days before reaching SMEAR III is shown for 6:00 h, 9:00
 134 h, 12:00 h and 15:00 h. The red shaded areas indicate the latitude/longitude pairs having the maximum
 135 residence time.



136

137 **Figure S4:** Diurnal variation of the inorganic clusters (a) and organic clusters (b) observed during
 138 the NPF event on 30 June 2019 as seen from the spectrum of CI-ApToF.

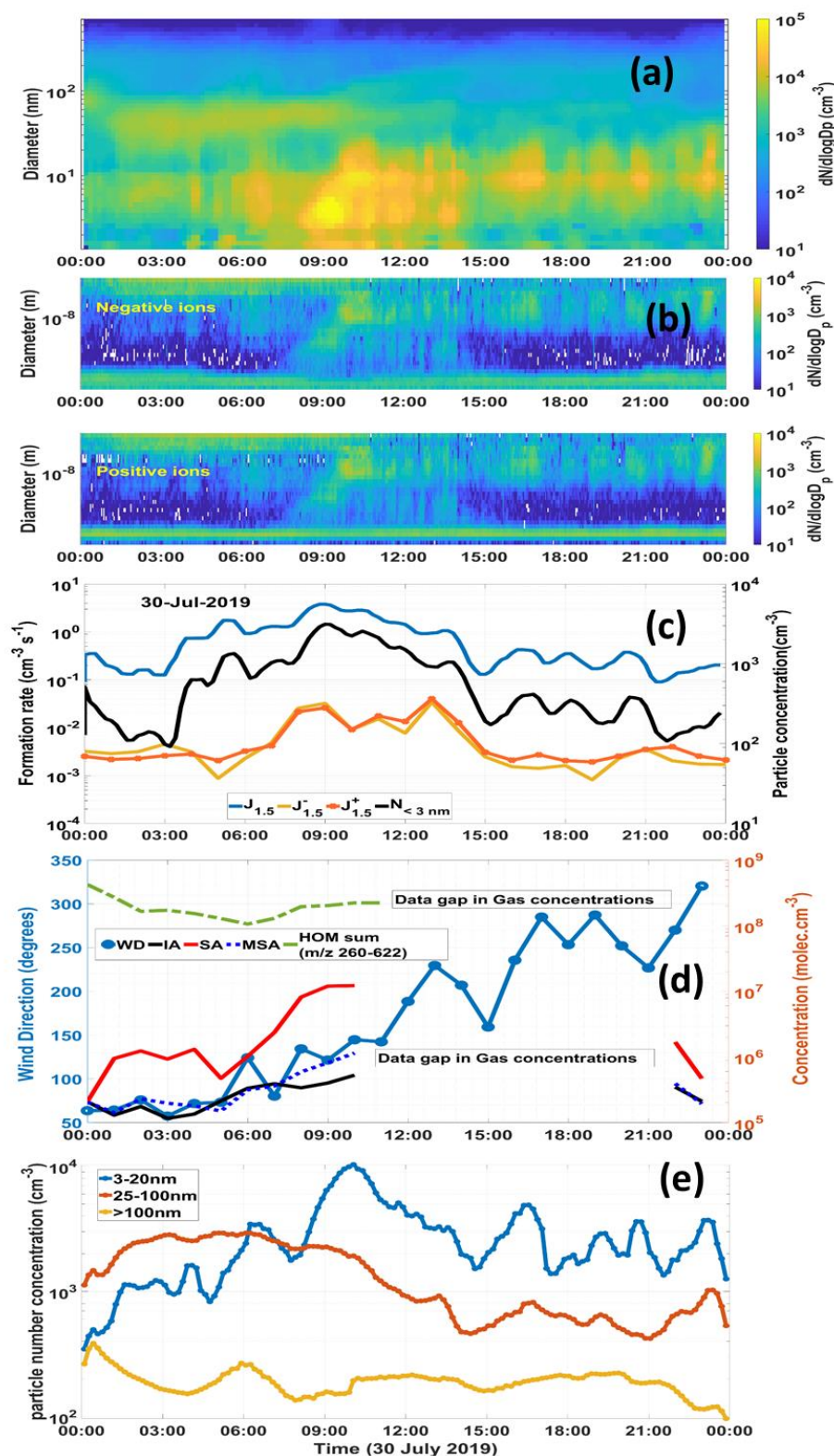
139

140 **Local/regional event 30 July 2019**

141 Another local/regional event was observed on 30 July 2019 (Fig. S5a), forming particles, which grew
142 to almost CCN relevant sizes. The growth of ions and particles actually occurred from 07:45 h-11:15
143 h (Fig. S5a and S5b). By this time, the particles had reached around 50 nm in size (lower limit of
144 CCN). The highest $J_{1.5}$ was $3.7 \text{ cm}^{-3} \text{ s}^{-1}$ was observed at 09:00 h, significantly higher than J (ions),
145 indicative of a neutral dominated nucleation event (Fig. S5c). After 11:30 h, we observe a group of
146 fragmented burst or spike events without clear growth pattern. No significant variation in formation
147 rates was observed in the positive and the negative mode (Fig. S5b). A clear increase in sub-3 nm
148 (1.25–3.1 nm) particle concentration (from 10^2 to $>10^3$) is seen during this event and formation rate
149 of the smallest particles ($J_{1.5}$) increases from $0.9 \text{ cm}^{-3} \text{ s}^{-1}$ to $3.8 \text{ cm}^{-3} \text{ s}^{-1}$ between 06:00 -09:00 h
150 indicating cluster formation (neutral nucleation) (Fig. S5c). A 10 times increase in sub 3nm particles
151 is observed once the cluster formation initiated (07:45 h, local time UTC+2 h) when the concentration
152 of SA increases from 8.2×10^6 to $1.2 \times 10^7 \text{ molec. cm}^{-3}$ and the nucleation mode particles how a
153 significant increase from $\sim 2000 \text{ cm}^{-3}$ to $\sim 10\,000 \text{ cm}^{-3}$ during the event, however we do not see any
154 significant increase in Aitken and accumulation mode particles (Fig. S5e). The aitken mode particle
155 concentration starts to increase after a time lag of 40 min. Unfortunately, in this case we cannot
156 discuss on the SA concentration after 12:00 h as data recording was disrupted between 12:30-20:30
157 h. The highest SA concentration during this event was $1.22 \times 10^7 \text{ molec cm}^{-3}$ as compared to IA and
158 MSA which were one order of magnitude lower than SA (1.15×10^6 and $5.28 \times 10^6 \text{ molec. cm}^{-3}$,
159 respectively) (Fig. S5d). The particles reached the size of 40 nm at around 11:30 h after which the
160 event ceases. The accumulation mode particles remain more or less constantly low, yet we observe a
161 disruption in the event. A change in wind direction from 120° to 200° was observed between 11:30–
162 12:30 h, which lead to the observation that we do not see regional NPF (growing particles) in the
163 changed air mass. The cyanobacteria bloom on 30 July 2019 was not much spread in the sea areas
164 (Fig. S5f).

165

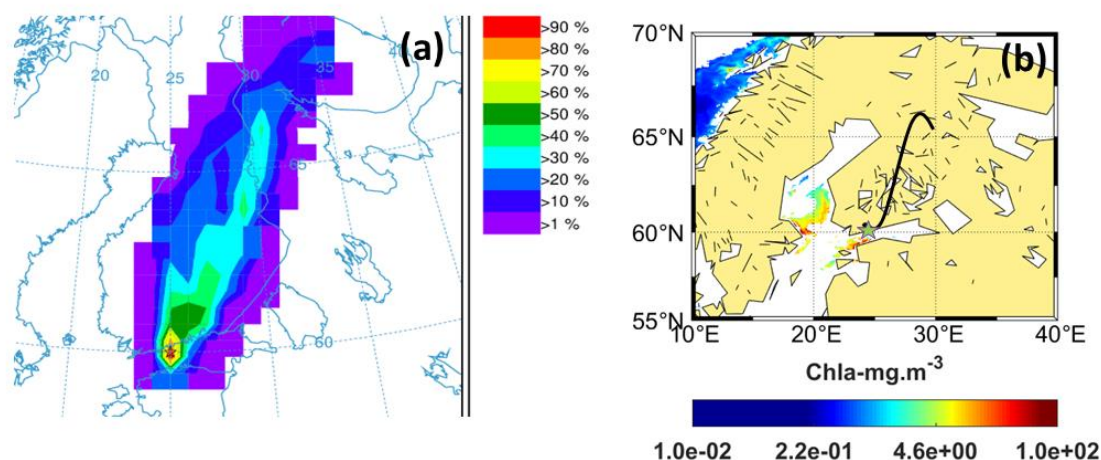
166



167

168 **Figure S5:** Local/regional Event, 30 July 2019. (a) Number size distribution of particles (data
 169 combined from PSM,NAIS and DMPS; size range: sub-3 nm–1000nm). (b) Charged particle number
 170 size distribution (negative: upper, positive: lower) obtained from the NAIS. (c) formation rates ($J_{1.5}$)
 171 of 1.5 nm particles and ions ($J_{1.5}^-$ and $J_{1.5}^+$) particle number concentrations (<3 nm). (d) Diurnal

172 variation of HOMs, SA, IA and MSA with wind direction (WD). (e) The concentration of nucleation
173 (3–10 nm) Aitken (10–100 nm) and accumulation mode (>100nm) particles during the event.

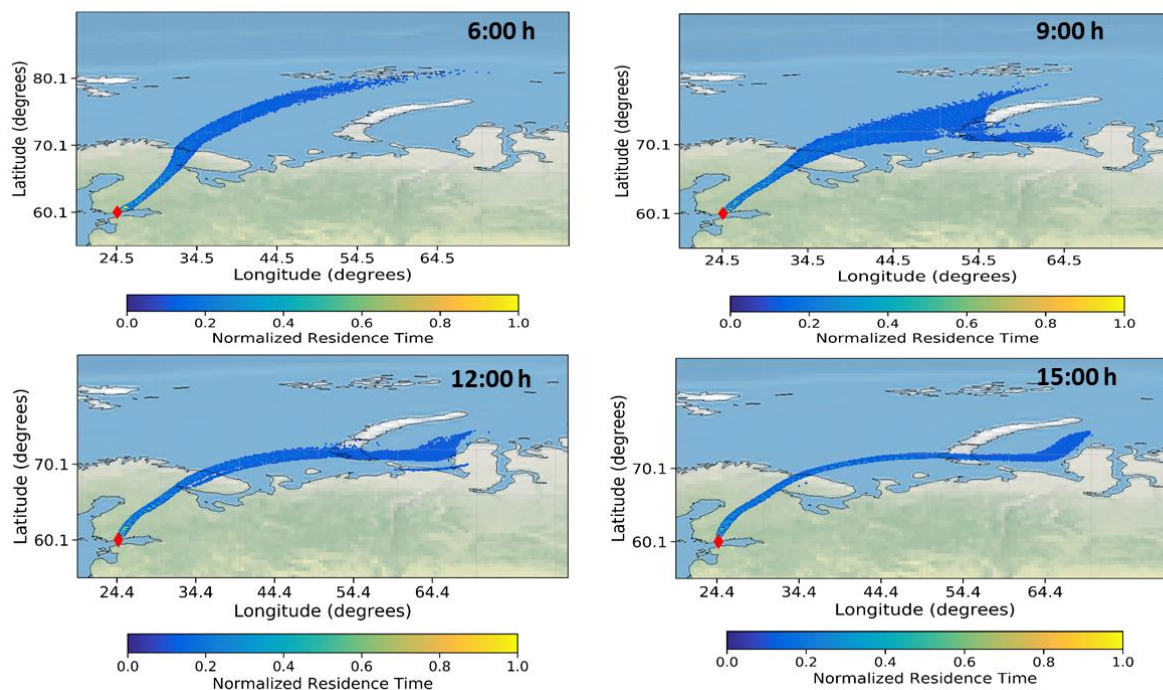


174

175 **Figure S6:** (a) Trajectory frequency plot (100 a.g.l, arrival time of trajectory at the measurement site:
176 22:00 h) for 24 h back trajectory using GDAS meteorological input data (frequency grid resolution:
177 $1.0^{\circ} \times 1.0^{\circ}$) (b) Chl-*a* concentrations (GlobColour level-3); Black line shows the trajectory direction
178 and the star point denotes the measurement site.

179

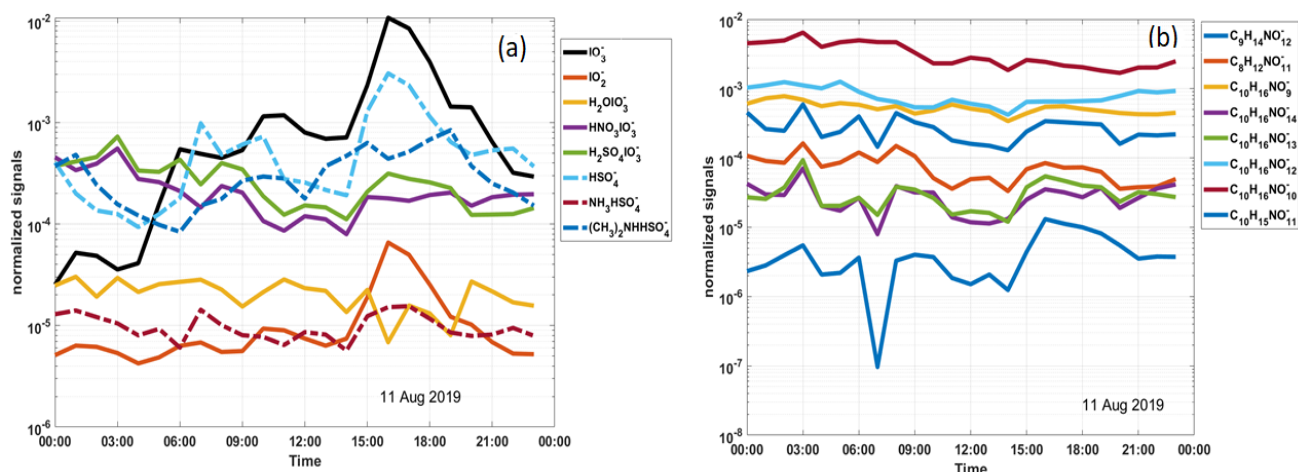
180 Even in lakes the abundance of cyanobacteria was sparse. Only cyanobacterial bloom was found in
181 Southern edge of Gulf of Bothnia and northern most part of the Baltic sea. The trajectory frequency
182 plots showed that most of the trajectories were from the northern land areas (including urban cities
183 and boreal forests) of Finland (Fig. S5f) with highest residence times over these land regions.
184 Therefore, the precursor gases from the biogenic origin, IA and MSA do not show a significant
185 concentration increase as compared to SA, during this event and hence their contribution towards the
186 initiation of the NPF event may not be as significant as SA. The greater residence times over the land
187 areas clearly support SA-driven NPF with possible contribution of organics.



188

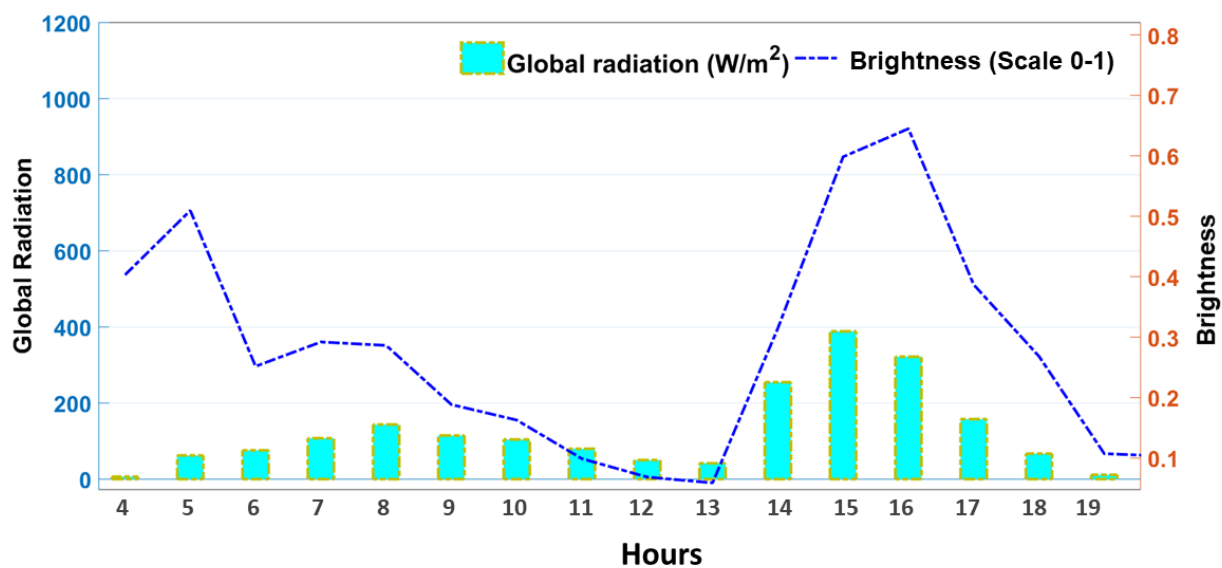
189 **Figure S7:** Normalized residence times of Air masses (3-day backwards) arriving at the experimental
 190 site on 30 July 2019. The color bar indicates the normalized residence times for each subplot. The
 191 residence time of particles originating 3 days before reaching SMEAR III is shown for 6:00 h, 9:00
 192 h, 12:00 h and 15:00 h. The red shaded areas indicate the latitude/longitude pairs having the maximum
 193 residence time. Note the highest residence times over the land areas.

194



195

196 **Figure S8:** Diurnal variation of the inorganic (a) and organic clusters (b) observed during the NPF
 197 event on 11 August 2019.

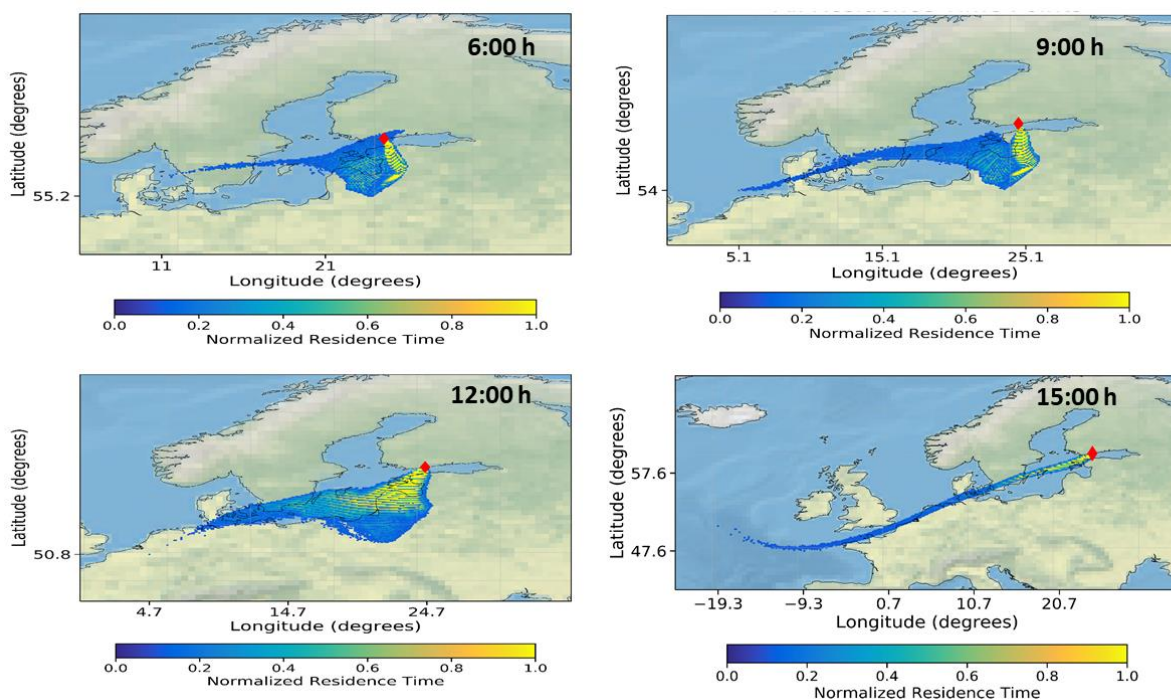


198

199 **Figure S9:** Diurnal variability of global radiation and estimated cloudiness on 11 August 2019.

200 Note the increased radiation and brightness from 14–16 h (time when NPF starts).

201



202

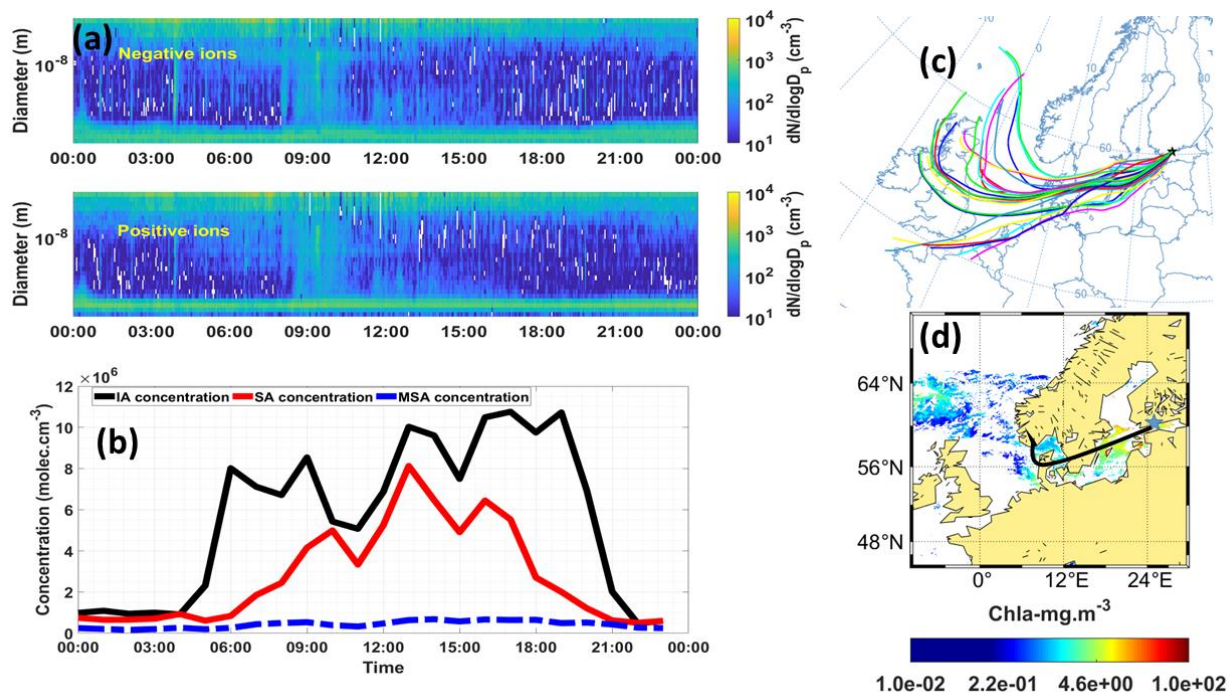
203 **Figure S10:** Normalized residence times of air masses (3-day backwards) arriving at the experimental

204 site on 11 August 2019. The color bar indicates the normalized residence times for each subplot. The

205 residence time of particles originating 3 days before reaching SMEAR III is shown for 6:00 h, 9:00

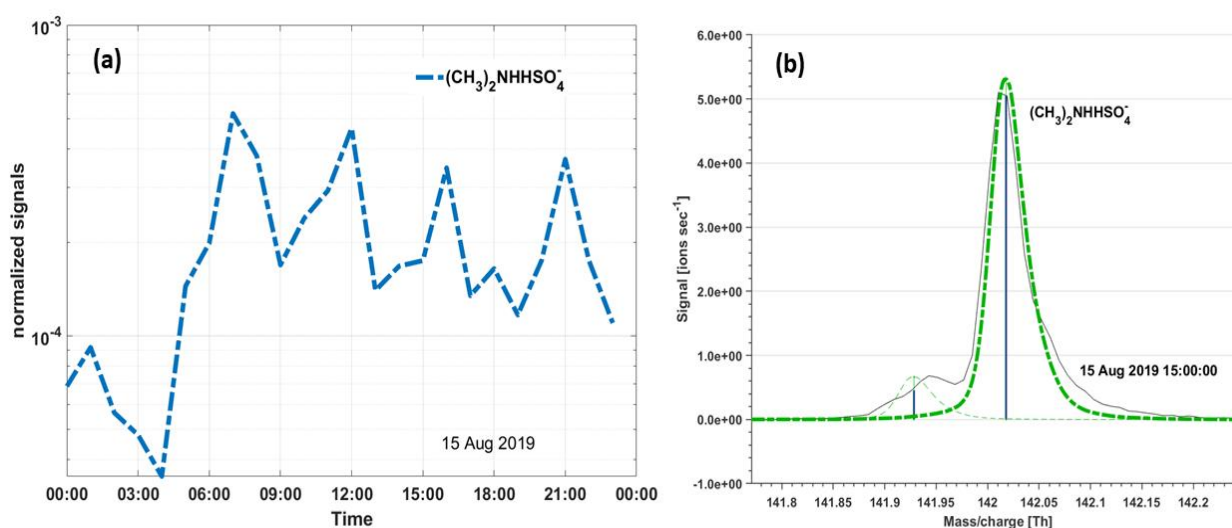
206 h, 12:00 h and 15:00 h. The red shaded areas indicate the latitude/longitude pairs having the maximum

207 residence time. Note the highest residence times over Baltic Sea region at 15:00 h (highest IA
 208 concentration was observed).



209

210 **Figure S11:** (a) Charged particle number size distribution (negative: upper, positive: lower) obtained
 211 from the NAIS. (b) concentration of SA, IA and MSA. (c) Trajectory analysis plot (100 a.g.l) for 24 h
 212 back trajectory using GDAS meteorological input data (frequency grid resolution: $1.0^\circ \times 1.0^\circ$) (d) Chl-
 213 *a* concentrations (GlobColour level-3) for 14 August 2019. Black line shows the trajectory direction
 214 and the star point denotes the measurement site.

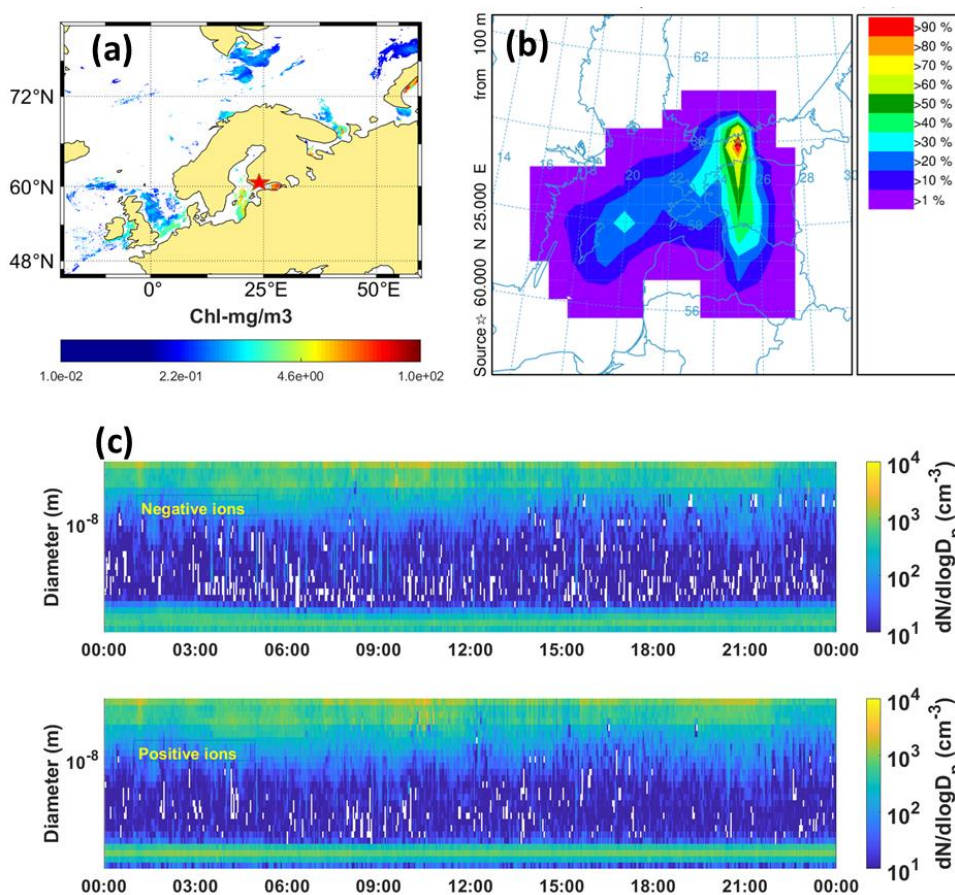


215

216 **Figure S12:** (a) Diurnal variation of the DMA-SA cluster (CI-ApiToF) observed during the NPF
 217 event on 15 August 2019. (b) The prominent peak of DMA-SA cluster seen at the peaktime of NPF
 218 at 15:00 h.

219

220



221

222 **Figure S13:** No event day, 17 August 2019 (a): Satellite map showing Chl_a concentrations
 223 (GlobColour level-3) (b) Trajectory analysis plot (100 a.g.l) for 24 h back trajectory using GDAS
 224 meteorological input data (frequency grid resolution: 1.0° × 1.0°). (c) Charged particle number size
 225 distribution (negative: upper, positive: lower) obtained from the NAIS.

226 References:

227 Beck, L. J., Sarnela, N., Junninen, H., Hoppe, C. J. M., Garmash, O., Bianchi, F., Riva, M., Rose, C., Peräkylä,
 228 O., Wimmer, D., Kausiala, O., Jokinen, T., Ahonen, L., Mikkilä, J., Hakala, J., He, X. C., Kontkanen,
 229 J., Wolf, K. K. E., Cappelletti, D., Mazzola, M., Traversi, R., Petroselli, C., Viola, A. P., Vitale, V.,
 230 Lange, R., Massling, A., Nøjgaard, J. K., Krejci, R., Karlsson, L., Zieger, P., Jang, S., Lee, K., Vakkari,
 231 V., Lampilahti, J., Thakur, R. C., Leino, K., Kangasluoma, J., Duplissy, E. M., Siivola, E., Marbouti,

232 M., Tham, Y. J., Saiz-Lopez, A., Petäjä, T., Ehn, M., Worsnop, D. R., Skov, H., Kulmala, M., Kerminen,
233 V. M. and Sipilä, M.: Differing Mechanisms of New Particle Formation at Two Arctic Sites, *Geophys.*
234 *Res. Lett.*, doi:10.1029/2020GL091334, 2021.

235 Dada, L., Lehtipalo, K., Kontkanen, J., Nieminen, T., Baalbaki, R., Ahonen, L., Duplissy, J., Yan, C., Chu,
236 B., Petäjä, T., Lehtinen, K., Kerminen, V. M., Kulmala, M. and Kangasluoma, J.: Formation and
237 growth of sub-3-nm aerosol particles in experimental chambers, *Nat. Protoc.*, 15(3), 1013–1040,
238 doi:10.1038/s41596-019-0274-z, 2020.

239 Dal Maso, M., Liao, L., Wildt, J., Kiendler-Scharr, A., Kleist, E., Tillmann, R., Sipilä, M., Hakala, J.,
240 Lehtipalo, K., Ehn, M., Kerminen, V. M., Kulmala, M., Worsnop, D. and Mentel, T.: A chamber study
241 of the influence of boreal BVOC emissions and sulfuric acid on nanoparticle formation rates at ambient
242 concentrations, *Atmos. Chem. Phys.*, 16(4), 1955–1970, doi:10.5194/acp-16-1955-2016, 2016.

243 Järvi, L., Hannuniemi, H., Hussein, T., Junninen, H., Aalto, P. P., Hillamo, R., Mäkelä, T., Keronen, P., Siivola,
244 E., Vesala, T. and Kulmala, M.: The urban measurement station SMEAR III: continuous monitoring of
245 air pollution and surface–atmosphere interactions in Helsinki, Finland. *Boreal Environ. Res.*, 14 (suppl.
246 A), 86–109, 2009. Kulmala, M., Petäjä, T., Nieminen, T., Sipilä, M., Manninen, H. E., Lehtipalo, K.,
247 Dal Maso, M., Aalto, P. P., Junninen, H., Paasonen, P., Riipinen, I., Lehtinen, K. E. J., Laaksonen, A.
248 and Kerminen, V. M.: Measurement of the nucleation of atmospheric aerosol particles, *Nat. Protoc.*,
249 7(9), 1651–1667, doi:10.1038/nprot.2012.091, 2012.

250 Lehtipalo, K., Kontkanen, J., Kangasluoma, J., Franchin, A., Wimmer, D., Schobesberger, S., Junninen, H.,
251 Petäjä, T., Sipilä, M., Worsnop, D. R., Kulmala, M., Lehtipalo, K., Mikkilä, J., Vanhanen, J., Leppä, J.
252 and Worsnop, D. R.: Methods for determining particle size distribution and growth rates between 1 and
253 3 nm using the Particle Size Magnifier, *Boreal Environ. Res.*, 19(September), 215–236, 2014.

254 Mangin, A. and d'Andon, O.F.: *GlobColour Product User Guide*, GC-UM-ACR-PUG-01, Version 4.1,
255 2017.

256 Nieminen, T., Lehtinen, K. E. J. and Kulmala, M.: Sub-10 nm particle growth by vapor condensation-effects
257 of vapor molecule size and particle thermal speed, *Atmos. Chem. Phys.*, doi:10.5194/acp-10-9773-2010,
258 2010.

259 Perez, R., Ineichen, P., Seals, R. and Zelenka, A.: Making full use of the clearness index for parameterizing
260 hourly insolation conditions, *Solar Energ.*, 45, 111–114, doi:10.1016/0038-092X(90)90036-C, 1990.

261 Pisso, I., Sollum, E., Grythe, H., Kristiansen, N. I., Cassiani, M., Eckhardt, S., Arnold, D., Morton, D.,
262 Thompson, R. L., Groot Zwaafink, C. D., Evangeliou, N., Sodemann, H., Haimberger, L., Henne, S.,
263 Brunner, D., Burkhardt, J. F., Fouilloux, A., Brioude, J., Philipp, A., Seibert, P. and Stohl, A.: The
264 Lagrangian particle dispersion model FLEXPART version 10.4, *Geosci. Model Dev.*, doi:10.5194/gmd-

265 12-4955-2019, 2019.

266 Rolph, G., Stein, A. and Stunder, B.: Real-time Environmental Applications and Display sYstem: READY,
267 Environ. Model. Softw., 95, 210–228, doi:10.1016/j.envsoft.2017.06.025, 2017.

268 Sánchez, G., Serrano, A., and Cancillo, M.: Effect of cloudiness on solar global, solar diffuse and terrestrial
269 downward radiation at Badajoz (Southwestern Spain), *Optica pura y aplicada*, 45, 33– 38, 2012.

270 Sogacheva, L., Saukkonen, L., Nilsson, E., Dal Maso, M., Schultz, D. M., De Leeuw, G., and Kulmala, M.:
271 New aerosol particle formation in different synoptic situations at Hyytiälä, southern Finland, *Tellus B*,
272 60, 485–494, doi:10.1111/j.1600- 0889.2008.00364.x, 2008.

273 Stein, A. F., Draxler, R. R., Rolph, G. D., Stunder, B. J. B., Cohen, M. D. and Ngan, F.: Noaa’s hysplit
274 atmospheric transport and dispersion modeling system, *Bull. Am. Meteorol. Soc.*, 96(12), 2059–2077,
275 doi:10.1175/BAMS-D-14-00110.1, 2015.

276 Stohl, A., Forster, C., Frank, A., Seibert, P. and Wotawa, G.: Technical note: The Lagrangian particle
277 dispersion model FLEXPART version 6.2, *Atmos. Chem. Phys.*, doi:10.5194/acp-5-2461-2005, 2005.

278 Stolzenburg, D., Stolzenburg, D., Simon, M., Ranjithkumar, A., Kürten, A., Lehtipalo, K., Lehtipalo, K.,
279 Gordon, H., Ehrhart, S., Finkenzeller, H., Pichelstorfer, L., Nieminen, T., He, X. C., Brilke, S., Xiao,
280 M., Amorim, A., Baalbaki, R., Baccharini, A., Beck, L., Bräkling, S., Murillo, L. C., Chen, D., Chu, B.,
281 Dada, L., Dias, A., Dommen, J., Duplissy, J., El Haddad, I., Fischer, L., Carracedo, L. G., Heinritzi, M.,
282 Kim, C., Kim, C., Koenig, T. K., Kong, W., Lamkaddam, H., Lee, C. P., Leiminger, M., Leiminger, M.,
283 Li, Z., Makhmutov, V., Manninen, H. E., Marie, G., Marten, R., Müller, T., Nie, W., Partoll, E., Petäjä,
284 T., Pfeifer, J., Philippov, M., Rissanen, M. P., Rissanen, M. P., Rörup, B., Schobesberger, S.,
285 Schuchmann, S., Shen, J., Sipilä, M., Steiner, G., Stozhkov, Y., Tauber, C., Tham, Y. J., Tomé, A.,
286 Vazquez-Pufleau, M., Wagner, A. C., Wagner, A. C., Wang, M., Wang, Y., Weber, S. K., Wimmer, D.,
287 Wimmer, D., Wlasits, P. J., Wu, Y., Ye, Q., Zauner-Wieczorek, M., Baltensperger, U., Carslaw, K. S.,
288 Curtius, J., Donahue, N. M., Flagan, R. C., Hansel, A., Hansel, A., Kulmala, M., Lelieveld, J., Volkamer,
289 R., Kirkby, J., Kirkby, J. and Winkler, P. M.: Enhanced growth rate of atmospheric particles from
290 sulfuric acid, *Atmos. Chem. Phys.*, doi:10.5194/acp-20-7359-2020, 2020.